14 Derivation of the mixing-layer height and detection of low-level jets by remote sensing

Stefan Emeis

Institute for Meteorology and Climate Research,

Atmospheric Environmental Research Division (IMK-IFU),

Karlsruhe Institute of Technology, Garmisch-Partenkirchen, Germany

14.1 Introduction

This chapter gives an overview of the derivation of mixing-layer height (MLH) and the detection of low-level jets (LLJs) by surface-based remote sensing instruments such as SODAR, LIDAR, ceilometer and RASS. The detection of vertical profiles indicating the structure of the atmospheric boundary layer (ABL) is one of the principal tasks of experimental boundary-layer research. MLH has become an important input parameter for the description of wind profiles above the surface layer (Gryning et al. 2007, Peña et al. 2010). LLJs are secondary wind maxima which occur at the top of a stable boundary layer. Over land, they are observed at several hundred metres above ground at night-time. Over the sea, they are found with offshore winds when warmer air flows over cooler water at the top of the shallow stable internal boundary layer at any time of the day. These shallow internal boundary layers are often considerably less than 100 m deep.

The next section describes methods to detect the mixing-layer height, while section 14.3 briefly mentions methods to capture the boundary-layer height. Section 14.4 gives more information on low-level jets. Acoustic (SODAR) and optical sounding techniques (LIDAR) have got a broad coverage elsewhere in this volume. RASS techniques are still quite unusual in the assessment of wind resources. Therefore, a subsection on technical details of this instrumentation has been added in section 14.2.3. A more complete survey of remote sensing instrumentation is given in Emeis (2010), an overview of applications of ground-based remote sensing is presented in Emeis (2011). The full scope of wind energy meteorology is presented in Emeis (2012).

14.2 Mixing-layer height

We must distinguish between the mixing-layer height, MLH (see section 14.2) and the boundary-layer height, z_i (see section 14.3). The boundary-layer height is the height up to which the influence of the presence of the lower surface is detectable. The mixing-layer height is the height up to which atmospheric properties (such as wind speed and turbulence) or substances originating from the surface are dispersed by turbulent vertical mixing processes. The mixing-layer – if it is present at all - is a part of the ABL. Thus, the mixing-layer height is usually shallower than the boundary-layer, but it fills the whole ABL in deep convective boundary layers.

Sometimes the terms mixed-layer height or mixing height are used as well for MLH, but we will stick here to the most common term mixing-layer height. The mixing-layer height is the height up to which atmospheric properties or substances originating from the Earth's surface or formed within this layer are dispersed almost uniformly over the entire depth of this layer by turbulent vertical mixing processes. Therefore, the existence and the height of a mixing layer can either be analyzed from a detection of the presence of the mixing process, i.e. turbulence, or from the verification that a given conservative atmospheric variable is distributed evenly over the full height range of the well-mixed layer. The level of turbulence can for instance be derived from fluctuations of the wind components or from temperature fluctuations. Suitable conservative atmospheric variables for the identification of the mixing layer and its height are, e.g., potential temperature, specific humidity or aerosol particle concentrations.

The latest rather complete overview of methods to determine MLH from in-situ measurements and surface-based remote sensing had been given by Seibert et al. (2000). Since then considerable development has taken place, especially concerning the usage of optical surface-based remote sensing methods (see the review paper by Emeis et al. (2008)) and RASS. This chapter will mainly follow this latter review.

Optical methods for MLH detection may be used to illustrate this recent progress. Seibert et al. (2000) still classified lidar methods as expensive, not eye-save, with a high lowest range gate, limited range resolution, and sometimes subject to ambiguous interpretation. This has changed drastically in the last ten years when better and smaller Doppler wind lidars have been built and the simpler non-Doppler ceilometers have been discovered to be a nearly ideal sounding instrument for the detection of the vertical structure of the boundary layer. Progress has been made in the field of acoustic sounding as well. Similarly, algorithms for the determination of MLH from vertical profiles of the acoustic backscatter intensity as described in Beyrich (1997) and Seibert et al. (2000) have been enhanced by using further variables available from sodar measurements such as the wind speed and the variance of the vertical velocity component (Asimakopoulos et al. 2004, Emeis and Türk 2004). Such enhancements had been named as possible methods in Beyrich (1995) and Seibert et al. (2000) but obviously no example was available at that time.

A variety of different algorithms have been developed by which the MLH is derived from ground-based remote sensing data (see Table 14.1 for a short overview). We will mainly concentrate on acoustic and optical remote sensing because electro-magnetic remote sensing has too high lowest range gates for a good coverage of shallow MLH. The disadvantage of a too high lowest range gate can partly be circumvented by slantwise profiling or conical scanning if the assumption of horizontal homogeneity can be made.

Table 14.1. Overview of methods using ground-based remote sensing for the derivation of the mixing-layer height mentioned in this Chapter (see rightmost column for section number)

method		short description	section
acoustic	ARE	analysis of acoustic backscatter intensity	14.2.1
"	HWS	analysis of wind speed profiles	14.2.1
"	VWV	analysis of vertical wind variance profiles	14.2.1
"	EARE	analysis of backscatter and vertical wind variance profiles	14.2.1
optical	threshold	detection of a given backscatter intensity threshold	14.2.2
"	gradient	analysis of backscatter intensity profiles	14.2.2
"	idealised backscatter	analysis of backscatter intensity profiles	14.2.2

“ wavelet	analysis of backscatter intensity profiles	14.2.2
“ variance	analysis of backscatter intensity profiles	14.2.2
acoust./electro-magn.	RASS	14.2.3
“	sodar-RASS and windprofiler-RASS	14.2.3
“ /in situ	sodar-RASS plus surface heat flux data	14.2.3
acoust./electro-magn.	sodar plus windprofiler	14.2.4
acoustic/optical	sodar plus ceilometer	14.2.4

14.2.1 Acoustic detection methods (SODAR)

Acoustic methods either analyze the acoustic backscatter intensity, or, if Doppler shifts in the backscattered pulses can be analyzed, features of vertical profiles of the wind components and its variances as well. The acoustic backscatter intensity is proportional to small-scale fluctuations in atmospheric temperature (usually generated by turbulence) or by stronger vertical temperature gradients. The latter feature may be an indication for the presence of temperature inversions, which can often be found at the top of the mixing layer.

Beyrich (1997) listed possible analyses which can mainly be made from acoustic backscatter intensities measured by a sodar. Later, Asimakopoulos et al. (2004) summarized three different methods to derive MLH from sodar data: (1) the horizontal wind speed method (HWS), (2) the acoustic received echo method (ARE), and (3) the vertical wind variance method (VWV). We will mainly follow this classification here and finally add a fourth method, the enhanced ARE method (EARE).

Fig. 14.1, showing an acoustic sounding taken in an Alpine valley, gives an impression what wealth of detailed vertical information can be derived from acoustic boundary-layer sounding. The left-hand frame displays the acoustic backscatter intensity and the right-hand frame the wind direction as time-height sections over one day (from midnight to midnight) and over a height range of 700 m. The depicted wintry situation from a day in January exhibits a multiple layering of the air in that valley due to the very stable thermal stratification of the valley air over a snow-covered valley floor. The multiple layering originated from an interlacing of down-valley (wind direction around 190°) and down-slope (wind direction around 230°) flows. The layers are separated by temperature inversions and each higher layer is potentially warmer than the next lower layer. They persisted nearly the whole day because no vertical mixing took place in the stably stratified valley atmosphere.

Acoustic received echo (ARE) method

The ARE method is the most basic method of determining MLH from acoustic remote sensing. Most of the methods listed in Beyrich (1997) belong to this method. The method does not require an analysis of the Doppler shift of the backscattered signals. The method makes use of the assumption that turbulence is larger in the mixing layer than in the atmosphere above, and that this turbulence is depicted in the intensity of the acoustic backscatter. MLH is analyzed either from the maximum negative slope or from the changing curvature of the vertical profile of the acoustic backscatter intensity or it is analyzed from the height where the backscatter intensity decreases below a certain pre-specified threshold value.

Horizontal wind speed (HWS) method

The HWS method requires the analysis of the Doppler shift of the backscattered acoustic signals. The algorithm is based on the analysis of the shape of hourly-averaged vertical wind speed profiles using the assumption that wind speed and wind direction are almost constant within the mixing layer but approach gradually towards the geostrophic values above the mixing layer. Beyrich (1997) listed this method in his Tab. 2 but did not discuss it further. The applicability of the method is probably limited to well-developed convective boundary layers (CBL) due to the underlying assumptions. Such CBL are often higher than the maximum range of a sodar. Even if the CBL height is within the range of the sodar the algorithm for the analysis of the Doppler shift often fails above the inversion topping the CBL due to too low signal-to-noise ratios. Today, small Doppler wind lidars are available to derive wind speed and direction profiles through the whole depth of the boundary layer. This facilitates the application of the HWS method.

Vertical wind variance (VWV) method

The VWV method is also working only for CBLs. It is based on the vertical profile of the variance of the vertical velocity component σ_w. In a CBL σ_w reaches a maximum in a height $a \cdot z_i$. Typical values for a are between 0.35 and 0.4. Thus, in principle, this is an extrapolation method. It has been tried for sodar measurements because it permits a detection of MLH up to heights which are 2.5 times above the limited maximum range (usually between 500 and 1000 m) of the sodar. Beyrich (1997) classified this method as not reliable. A related method, which is based on power spectra of the vertical velocity component, is integrated in the commercial evaluation software of certain SODARs (Contini et al. 2009). The application of the VWV method is now also been facilitated by the easy availability of small Doppler wind lidars.

Enhanced acoustic received echo (EARE) method

The EARE algorithm has been proposed by Emeis and Türk (2004) and Emeis et al. (2007). The method is an enhancement of the ARE method in two ways. Firstly, it includes further variables into the MLH algorithm that are available from Doppler-sodars. The benefits of the additional usage of the variance of the vertical velocity component have been demonstrated by Emeis and Türk (2004). Secondly, it determines not only MLH from sodar measurements but also the heights of additional lifted inversions. Especially in orographically complex terrain, the vertical structure of the ABL can be very complicated. Emeis et al. (2007) have shown that several persistent inversions one above the other which form in deep Alpine valleys can be detected from sodar measurements (Fig. 14.1).

EARE determines three different types of heights based on acoustic backscatter intensity and the variance of the vertical velocity component. Because the horizontal wind information above the inversion is not regularly available from SODAR measurements, horizontal wind data have not been included into this scheme. In the following a letter "H" and an attached number will denote certain derived heights which are related to inversions and the MLH; while the variable z is used to denote the normal vertical coordinate. The EARE algorithm detects:

- the height ($H1$) of a turbulent layer characterised by high acoustic backscatter intensities $R(z)$ due to thermal fluctuations (therefore having a high variance of the vertical velocity component σ_w),
- several lifted inversions ($H2\_n$) characterized by secondary maxima of acoustic backscatter due to a sharp increase of temperature with height and simultaneously low σ_w (like those depicted in the left-hand frame of Fig. 14.1), and

- the height of a surface-based stable layer (*H3*) characterised by high backscatter intensities due to a large mean vertical temperature gradient starting directly at the ground and having a low variance of the vertical velocity component.

The height *H1* corresponds to a sharp decrease $\partial R/\partial z < DR_1$ of the acoustic backscatter intensity *R(z)* below a threshold value R_c with height *z* usually indicating the top of a turbulent layer:

$$H1 = z, \text{ if } (R(z) < R_c \text{ and } R(z+1) < R(z) + z\, DR_1 \text{ and } R(z+2) < R(z) + 2\, z\, DR_1) \qquad (14.1)$$

R_c = 88 dB and DR_1 = -0.16 dB/m have proven to be meaningful values in the abovementioned studies. R_c is somewhat arbitrary because the received acoustic backscatter intensities from a SODAR cannot be absolutely calibrated. An absolute calibration would require the knowledge of temperature and humidity distributions along the sound paths for a precise calculation of the sound attenuation in the air. DR_1 is, at least for smaller vertical distances, independent from the absolute value of R_c. An application-dependent fine-tuning of R_c and DR_1 may be necessary.

Elevated inversions are diagnosed from secondary maxima of the backscatter intensity that are not related to high turbulence intensities. For elevated inversions increase in backscatter intensity below a certain height *z = H2* and a decrease above is stipulated while the turbulence intensity is low:

$$H2\_n = z, \text{ if } (\partial R/\partial z|_{z+1} < -DR_2 \text{ and } \partial R/\partial z|_{z-1} > DR_2 \text{ and } \sigma_w < 0.70 \text{ ms}^{-1}) \qquad (14.2)$$

for *n = 1, …, N*. In Emeis et al. (2007) *N* was chosen to be five. A threshold value DR_2 = 0.08 dB/m has proven suitable. But again, an application-dependent tuning may be advisable.

The determination of the height of the stable surface layer *H3* is started if the backscatter intensity in the lowest range gates is above 105 dB while σ_w is smaller than 0.3 ms^{-1}. The top of the stable layer *H3* is at the height where either the backscatter intensity sinks below 105 dB or σ_w increases above 0.3 ms^{-1}.

$$H3 = z, \text{ if } (R(z) > 105 \text{ dB and } R(z+1) < 105 \text{ dB and } \sigma_w(z) < 0.3 \text{ ms}^{-1}) \text{ or if } (\sigma_w(z) < 0.3 \text{ ms}^{-1} \text{ and } \sigma_w(z+1) > 0.3 \text{ ms}^{-1} \text{ and } R(z) > 105 \text{ dB}) \qquad (14.3)$$

The σ_w values used in Eqs. (14.2) and (14.3) have been determined by optimizing the automatic application of the detection algorithm. In doing so it turned out that no lifted inversions occurred with a variance σ_w higher than 0.7 ms^{-1} and that the variance σ_w in nocturnal stable surface layers was always below 0.3 ms^{-1}. The first σ_w threshold made it possible to distinguish between inversions and elevated layers of enhanced turbulence. The latter σ_w threshold made it possible to differentiate between nocturnal stable surface layers and daytime super-adiabatic surface layers although both types of surface layers yield more or less the same level of backscatter intensity. Finally MLH from the acoustic remote sensing is determined as the minimum of *H1*, *H2_1*, and *H3*:

$$MLH_{ac} = \min (H1, H2\_1, H3) \qquad (14.4)$$

14.2.2 Optical detection methods

Usually the aerosol content of the mixing layer is higher than in the atmospheric layer above, because the emission sources for aerosol are in most cases on the ground. Aerosol formation from precursors mainly takes place near the surface as well. Making the assumption that the vertical aerosol distribution adapts rapidly to the changing thermal structure of the boundary layer, MLH can

be determined from the analysis of the vertical aerosol distribution. This also includes the assumption that the vertical aerosol distribution is not dominated by horizontally advected aerosol plumes or layers. The heights of the near surface aerosol layers (*H4_n*) can be analysed from the optical vertical backscatter profile obtained from optical remote sensing. Several methods have been developed, the most prominent of these being: (1) the threshold method, (2) the gradient or derivative method, (3) the idealised gradient method, (4) the wavelet method, and (5) the variance method. In addition, the horizontal wind speed method and the vertical wind variance method mentioned in Section 14.2.1 above are available to derive the vertical structure of the boundary layer from Doppler wind lidar data.

The application of optical remote sensing for MLH determination has focussed on the use of ceilometers in recent years. Ceilometers can be regarded as a small lidar. They are simpler and they have a much lower lowest range gate than lidars. For the detection of MLH below 150 to 200 m a ceilometer with one optical axis for the emitted and the received beam should be used. Due to the thin light beams the overlap of the emitted and received beam from a ceilometer with two parallel optical axes can be insufficient in this height range. Further on, Doppler shifts are not analyzed by ceilometers. Therefore, in contrast to acoustic remote sensing with Doppler-Sodars, additional variables in addition to the backscatter intensity are not available from ceilometers for the design of determination schemes for MLH. Thus the schemes listed below all resemble to the ARE methods for acoustic remote sensing.

Fig. 14.2 shows a sample measurement with a mono-axial ceilometer. The left-hand frame displays the optical backscatter intensity and the right-hand frame the negative vertical derivative of this intensity as time-height sections over one day (from midnight to midnight) and over a height range of 2000 m. The data was received on a clear day in spring and the vertical structure of the ABL was dominated by surface heating due to incoming solar radiation during daytime and radiative surface cooling during night-time. In the morning hours until about 9 a.m. a shallow stable nocturnal surface layer with a depth of about 200 m and a residual layer with a depth of about 1200 to 1400 m can be distinguished. From 9 a.m. onwards the evolution of a daytime convective boundary layer with a maximum depth of about 1400 m can be clearly seen. The dots in both frames of Fig. 14.2 indicate the mixing-layer height determined with the gradient method described below. The right-hand frame in Fig. 14.2 demonstrates that the analysed MLH values indeed coincide with maxima of the negative vertical gradient of the optical backscatter intensity.

Threshold method

Melfi et al. (1985) and Boers et al. (1988) used simple signal threshold values, though this method suffers from the need to define them appropriately (Sicard et al. 2006). *H4* is defined here as the height within the vertical profile of the optical backscatter intensity where the backscatter intensity first exceeds a given threshold when coming downward from the free unpolluted troposphere. The determination of several heights *H4_n* would require the definition of several thresholds which probably cannot be done a priory to the analysis. Therefore this will always lead to a subjective analysis of MLH. The left-hand frame in Fig. 14.2 shows that the threshold value cannot be kept constant during the diurnal evolution of the boundary layer in order to get a result which is comparable to the one from the gradient method applied in Fig. 14.2.

Gradient or derivative methods

Hayden et al. (1997) and Flamant et al. (1997) proposed to use the largest negative peak of the first derivative of the optical attenuated backscatter intensity ($B(z)$) for the detection of $H4$ from LIDAR data (height of gradient minimum $H4_{GM}$):

$$H4_{GM} = min(\partial B(z)/\partial z) \qquad (14.5)$$

The right-hand frame of Fig. 14.2 demonstrates that this is a very meaningful assumption. Likewise Wulfmeyer (1999) used the first minimum of the slope to detect the top of a convective boundary layer from DIAL data. Münkel and Räsänen (2004) and Schäfer et al. (2004, 2005) applied the gradient method to ceilometer data. Menut et al. (1999) took the minimum of the second derivative of $B(z)$ as the indication for MLH:

$$H4_{IPM} = min(\partial^2 B(z)/\partial z^2) \qquad (14.6)$$

This method is called inflection point method (IPM). It usually gives slightly lower values for $H4$ than the gradient method in Eq. (14.5). A further approach was suggested by Senff et al. (1996). They looked for the largest negative gradient in the logarithm of the backscatter intensity (height of logarithmic gradient minimum $H4_{LGM}$):

$$H4_{LGM} = min(\partial lnB(z)/\partial z) \qquad (14.7)$$

This approach usually gives the largest value for $H4$. According to Sicard et al. (2006) $H4_{IPM}$ from Eq. (14.6) is closest to the MLH derived from radiosonde ascents via the Richardson method. The other two algorithms in Eqs. (14.5) and (14.7) give slightly higher values.

In Emeis et al. (2007) the gradient method in Eq. (14.5) has been further refined and extended to enable the calculation of up to $n=5$ lifted inversions. This algorithm, which has also been used for the MLH analysis shown in Fig. 14.2, is described in the following. Prior to the determination of gradient minima the overlap and range corrected attenuated backscatter profiles have to be averaged over time and height to suppress noise generated artefacts. Therefore the $H4$ values are determined in a two-step procedure. Between 140 m and 500 m height sliding averaging is done over 15 min and a height interval Δh of 80 m. In the layer between 500 and 2000 m Δh for vertical averaging is extended to 160 m. Two additional parameters have been introduced to further reduce the number of false hits. The minimum accepted attenuated backscatter intensity B_{min} right below a lifted inversion is set to $200*10^{-9}$ $m^{-1}sr^{-1}$ in the lower layer and $250*10^{-9}$ $m^{-1}sr^{-1}$ in the upper layer. Additionally the vertical gradient value $\partial B/\partial z_{max}$ of a lifted inversion must be more negative than -$0.30*10^{-9}$ $m^{-2}sr^{-1}$ in the lower layer and more negative than -$0.60*10^{-9}$ $m^{-2}sr^{-1}$ in the upper layer.

If $B(z)$ denotes the measured attenuated backscatter intensity in the height z above ground averaged over time and height and Δh is the height averaging interval, then the gradient $\partial B/\partial z$ in the height z is calculated as

$$\partial B/\partial z|_z = (B(z+\Delta h/2) - B(z-\Delta h/2)) / \Delta h \qquad (14.8)$$

A gradient minimum is characterized by a change of sign from minus to plus of the second derivative of $B(z)$. The height interval under examination is searched from bottom to top for these gradient minima $H4\_n$.

The second derivative of $B(z)$ in the height z is

$\partial^2 B/\partial z^2|_z = (\partial B/\partial z\ |_{z+\Delta h/2} - \partial B/\partial z\ |_{z-\Delta h/2}) / \Delta h.$ (14.9)

There is a gradient minimum *H4_n* in the height *z* if the second derivative of *B(z)* one range gate below *z* is not positive, if the second derivative of *B(z)* in the height *z* is positive, and if the false hit conditions mentioned above are fulfilled:

H4_n = z, if $\partial^2 B/\partial z^2|_{z-1} \leq 0$ and $\partial^2 B/\partial z^2|_z > 0$ and $B(z-\Delta h/2) \geq B_{min}$ and $\partial B/\partial z\ |_z \leq \partial B/\partial z_{max}$ for n = 1, …, 5. (14.10)

The MLH from optical remote sensing is taken as the lowest height *H4_n*:

$MLH_{op} = H4\_1$ (14.11)

Idealised backscatter method

A parallel development by Eresmaa et al. (2006) using an idealised backscatter profile, originally described by Steyn et al. (1999), is also an extension of the gradient method. MLH is not determined from the observed backscatter profile, but from an idealised backscatter profile fitted to the observed profile. The robustness of this technique is founded on utilising the whole backscatter profile rather than just the portion surrounding the top of the mixing layer. In this method an idealized backscattering profile $B_i(z)$ is fitted to measured profile by the formula

$B_i(z) = (B_m + B_u) / 2 - (B_m - B_u) / 2\ erf ((z - h)/\Delta h)$ (14.12)

where B_m is the mean mixing layer backscatter, B_u is the mean backscatter in air above the mixing layer and *Δh* is related to the thickness of the entrainment layer capping the ABL in convective conditions. Two new parameters *A1* and *A2* are defined so that *A1=(B_m+B_u)/2* and *A2=(B_m−B_u)/2*. The value of *A1* is kept constant during the fitting procedure. A good estimation of *A1* based on an initial order-of-magnitude guess for the MLH is crucial for the quality of the result.

Wavelet method

A Wavelet method has been developed for the automatic determination of mixing layer height from backscatter profiles of an LD-40 ceilometer by de Haij et al. (2006). Before that wavelet transforms have been applied in recent studies for MLH determination from LIDAR observations (e.g. Cohn and Angevine, 2000; Davis et al., 2000; Brooks, 2003; Wulfmeyer and Janjić 2005). The most important advantage of wavelet methods is the decomposition of the signal in both altitude as well as vertical spatial scale of the structures in the backscatter signal.

The Wavelet algorithm in de Haij et al. (2006) is applied to the 10 minute averaged range and overlap corrected backscatter profile *B(z)* within a vertical domain of 90 − 3000 m. For each averaged profile the top of two significant aerosol layers are detected in order to detect MLH as well as the top of a secondary aerosol layer, like e.g. an advected aerosol layer or the residual layer. This Wavelet MLH method uses the scale averaged power spectrum profile $W_B(z)$ of the wavelet transform with 24 dilations between 15 and 360 m and step size 15 m. The top of the first layer, *H4_1*, is detected at the first range gate at which the scale averaged power spectrum $W_B(z)$ shows a local maximum, exceeding a threshold value of 0.1. This threshold value is empirically chosen, based on the analysis of several cases with both well pronounced and less clearly pronounced mixing layer tops. *H4_2* is optionally determined in the height range between *H4_1* and the upper boundary of detection. A

valid *H4_2* is detected at the level with the strongest local maximum of $W_B(z)$ provided that this maximum is larger than the $W_B(z)$ of *H4_1*. MLH is set equal to *H4_1*.

However, problems with this method arise e.g. in case of multiple (well defined) aerosol layers, which renders the selection of the correct mixing layer top ambiguous. Furthermore, in spring and summer the detection of the MLH for deep (convective) boundary layers often fails. This is mostly due to the high variability of the aerosol backscatter signal with height which limits the range for MLH estimation in those conditions (de Haij et al. 2006).

Variance method

At the top of the convective boundary layer (CBL) we have entrainment of clear air masses from the free troposphere into the ABL. The entrainment process is temporarily variable and leads locally to considerable fluctuations in the aerosol concentration. Therefore the maximum in the vertical profile of the variance of the optical backscatter intensity can be an indicator for an entrainment layer on top a CBL (Hooper and Eloranta 1986, Piironen and Eloranta 1995). The method is called variance centroid method in Menut et al. (1999). The variance method for the CBL height is also described in Lammert and Bösenberg (2006). Due to the assumptions made this method is suitable for daytime convective boundary layers only. An elucidating comparison between the gradient method and the variance method can be found in Martucci et al. (2004) although they used a Nd:YAG LIDAR at 532 nm instead of a ceilometer and thus suffered from a high lowest range gate in the order of 300 m.

14.2.3 RASS

The acoustic and optical methods for MLH determination, which have been described in the sections above, are all indirect methods that try to infer the mixing-layer height from other variables which usually adapt to the vertical structure of the ABL. The only direct and key variable for the analysis of the presence of a mixing layer is the vertical profile of virtual temperature. Temperature profiles can directly be measured with a radio-acoustic sounding system (RASS). Fig. 14.3 shows an example. We start here with a short description of the available RASS methods.

Instrumentation

A radio-acoustic sounding system (RASS) operates acoustic and electro-magnetic sounding simultaneously (Marshall et al. 1972). This instrument is able to detect acoustic shock fronts of the acoustic pulses and to determine their propagation speed from the Doppler shift of the backscattered electro-magnetic waves. This propagation speed is equal to the speed of sound which in turn is a known function of air temperature and humidity. To different types of RASS have been realised (Engelbart and Bange 2002): a Bragg-RASS and a Doppler-RASS.

Bragg-(windprofiler) RASS

A Bragg-RASS (or windprofiler-RASS) is basically a windprofiler with an additional acoustic emitter. When the Bragg condition is fulfilled (Fig. 14.4), i.e. the wavelength of the sound waves λ_a is half the one of the electro-magnetic waves λ_e, then there is optimal backscatter of the electro-magnetic waves from the acoustic waves (Fig. 14.5). The electro-magnetic signal is emitted at a fixed frequency, but the emitted sound signal is a chirp signal with varying frequency f_a. From the sound wave length $\lambda_{a,B}$ at which optimal backscatter occurs the propagation speed of the sound signal can be determined via the following dispersion relation:

$c_a = \lambda_{a,B} / 2 * f_a$ (14.13)

For a VHF windprofiler operating at 50 MHz a sound frequency of about 100 Hz is used, for a UHF windprofiler operating at 1 GHz a sound frequency around 2 kHz is most suitable to fulfil the Bragg condition. Because the attenuation of sound waves in the atmosphere is strongly frequency dependent, a UHF RASS can detect temperature profiles up to about 1.5 km height whereas a VHF RASS can observe temperature profiles throughout the troposphere.

Doppler-(sodar) RASS

A Doppler-RASS (or sodar-RASS) is a sodar with an additional electro-magnetic emitter and receiver (Fig. 14.6) operating at a frequency $f_{e,0}$. From the Doppler shift Δf_e of the electro-magnetic radiation which is backscattered at the density fluctuations caused by the sound waves the propagation speed c_a of the sound waves is determined:.

$c_a = - 0,5 \, c * \Delta f_e / f_{e,0}$). (14.14)

c denotes the speed of light. A Doppler-RASS like a Bragg-RASS also emits a chirp sound signal in order to assure that the Bragg condition is optimally met due to the varying temperature over the entire height range.

The so determined propagation speed c_a is a sum of the speed of sound c_s and of the vertical movement of the air w within which the sound waves propagate:

$c_a = c_s + w$ (14.15)

The vertical air speed component w can be determined separately from the Doppler shift of the backscattered electro-magnetic clear-air signal when operating a Bragg-RASS or from the Doppler shift of the backscattered acoustic signal when operating a Doppler-RASS. Using the definition of the acoustic temperature the height profile of c_s can then be converted in a height profile of the acoustic temperature T_a. For many purposes this acoustic temperature is a sufficiently accurate approximation of the virtual air temperature. The maximum range of a sodar-RASS is usually less than thousand metres so that such an instrument covers the lower part of the boundary layer. Due the high vertical resolution and the low minimum range of about 30 to 40 m, which is comparable to the abilities of a sodar, a sodar-RASS is well suited for the detection of shallow nocturnal boundary layers.

Algorithms

MLH can be determined from the lowest height where the vertical profile of potential temperature increases with height indicating stable thermal stratification of the air. The great advantage of RASS measurements is that the magnitude of stability (inversion strength) can be assessed quantitatively which is not possible from the acoustic and optical sounding devices described before. Fig. 14.3 displays a time-height cross-section of potential temperature over three days starting at midnight for a height range of 540 m. On the afternoons of the second and the third day well-mixed boundary layers formed, which can be deduced from the vertically constant potential temperature. New surface layers form on the evenings of all three days at about 6 p.m. The depth of these new surface layers increase during the night to about 200 to 300 m. Above these nocturnal surface layers low-level jets (see below) form, indirectly visible from the white areas indicating missing data in Fig. 14.3.

Stronger winds like those in low-level jets blow the sound pulses from the RASS out of the focus of the electro-magnetic antenna and hence lead to a failure of the temperature detection.

Ideally, thermal stratification of air should be analyzed from the virtual potential temperature ($\vartheta_v = \vartheta (1 + 0.609\, q)$), where q is specific humidity) in order to include the effects of the vertical moisture distribution on the atmospheric stability. Unfortunately, no active remote sensing device for the determination of high-resolution moisture profiles is available. Therefore, the acoustic potential temperature ($\vartheta_a = \vartheta (1 + 0.513\, q)$), which actually is the temperature that is delivered by a RASS, is often used as a substitute. This is sufficient for cold and dry environments, but somewhat underestimates the virtual potential temperature in humid and warm environments. In case of larger vertical moisture gradients and small vertical temperature gradients this can lead to a switch in stability from stable to unstable or vice versa.

Engelbart and Bange (2002) have analyzed the possible advantages of the deployment of two RASS instruments, a sodar-RASS and a high-UHF windprofiler-RASS, to derive boundary layer parameters. With these instruments, in principle, MLH can either be determined from the temperature profiles or from the electro-magnetic backscatter intensity. The latter depends on temperature and moisture fluctuations in the atmosphere. The derivation of MLH from the temperature profile requires a good vertical resolution of the profile which is mainly available only from the sodar-RASS. But even if the inversion layer at the top of the boundary layer is thick enough, due to the high attenuation of sound waves in the atmosphere, also the 1290 MHz-windprofiler-RASS used by Engelbart and Bange (2002) can measure the temperature profile only up to about 1 km. Therefore, in the case of a deeper CBL, MLH was determined from a secondary maximum of the electro-magnetic backscatter intensity which marks the occurrence of the entrainment zone at the CBL top. Thus, with this instrument combination the whole diurnal cycle of MHL is ideally monitored by interpreting the temperature profile from the sodar-RASS at night-time and by analyzing the electro-magnetic backscatter intensity profile from the windprofiler-RASS during daytime.

Hennemuth and Kirtzel (2008) have recently developed a method that uses data from a sodar-RASS and surface heat flux data. MLH is primarily detected from the acoustic backscatter intensity received by the sodar part of the sodar-RASS and verified from the temperature profile obtained from the RASS part of the instrument. Surface heat flux data and statistical evaluations complement this rather complicated scheme. The surface heat flux is used to identify situations with unstable stratification. In this respect this observable takes over an analogous role as the σ_w in the EARE algorithm (see section 14.2.1). The results have been tested against radiosonde soundings. The coincidence was good in most cases except for a very low MLH at or even below the first range gate of the sodar and the RASS.

14.2.4 Further techniques

Beyrich and Görsdorf (1995) have reported on the simultaneous usage of a SODAR and a wind profiler for the determination of MLH. For the SODAR data the ARE method was used. From the wind profiler data MLH was likewise determined from the height of the elevated signal intensity maximum (see also Angevine et al. 1994, Grimsdell and Angevine 1998, White et al. 1999). Good agreement between both algorithms was found for evolving convective boundary layers. The vertical ranges of the two instruments (50 to 800 m for the SODAR and 200 to 3000 m for the wind profiler) allowed following the complete diurnal cycle of MLH.

14.2.5 Comparison of acoustic and optical MLH detection algorithms

There is an interesting difference between the schemes for the determination of MLH from acoustic and optical backscatter intensities which should be noted carefully. While the acoustic backscatter intensity itself is taken for the detection of *H1* and *H3* (see Eqs. (14.1) and (14.3)) and the first derivative of this backscatter intensity for the determination of *H2* (see Eq. (14.2), the first and the second derivative of the optical backscatter intensity (but not the optical backscatter intensity itself) is used to determine *H4* (see Eq. (14.5)). This discrepancy in the processing of the two backscatter intensities is due to the different scattering processes for acoustic and optical waves: Acoustic waves are scattered at atmospheric refractivity gradients and thus at temperature gradients (Neff and Coulter 1986) while optical waves are scattered at small particles. Therefore the optical backscatter intensity is proportional to the aerosol concentration itself. The MLH on the other hand, which we desire to derive from these backscatter intensities, is in both cases found in heights where we have vertical gradients of the temperature and of the aerosol concentration. Therefore, in principle, the vertical distribution of the acoustic backscatter intensity should look very much alike the vertical distribution of the vertical gradient of the optical backscatter intensity.

Simultaneous measurements with different remote sensing devices have mainly been made in order to evaluate one remote sensing method against the other (Devara et al. (1995)). But one could also think of combining the results two or more remote sensing devices for determining the structure of the ABL. The analysis of the sodar data and the ceilometer data can be combined to one single piece of MLH information by forming the minimum from Eqs. (14.4) and (14.11):

$$\text{MLH} = \min(\text{MLH}_{ac}, \text{MLH}_{op}) \qquad\qquad (14.16)$$

14.3 Boundary layer height

Often, the boundary layer consists of more layers than just the mixing layer. For example, at night, a residual layer may persist over a newly formed near-surface stable surface layer. The deployment of larger lidars (Bösenberg and Linné 2002) or modern small wind lidars may be the first choice today to detect such features. The combined deployment of a sodar and a ceilometer is possible as well. Such a combination of parallel measurements of the vertical structure of the atmospheric boundary layer by a ceilometer and a sodar is described in Emeis and Schäfer (2006). Fig. 14.7, which is taken from this study, shows a daytime convective boundary layer, shallow nocturnal surface layers in the morning and the evening, and a residual layer above the nocturnal surface layers. The ceilometer detects the overall boundary layer height (blue triangles) whose height is partly modified by large-scale sinking motion in the anticyclone dominating the weather during the measurement period. Stable nocturnal surface layers with a depth of a few hundred metres can be detected underneath the black squares derived from the sodar soundings. The convective boundary layer during daytime fills the full depth of the boundary layer. This combination offers the same advantages as the combination of sodar and windprofiler presented in Beyrich and Görsdorf (1995). First results from a combined deployment of a RASS and a ceilometer are given in Emeis et al. (2009).

In such combined remote sensing measurements a sodar better detects the near-surface features such as nocturnal stable layers (a RASS instead of a sodar directly delivers the near-surface temperature profile) while the ceilometer is able to follow the diurnal variation of the daytime

convective boundary layer and the top of the whole boundary layer. The residual layer then becomes visible as the layer between the new nocturnal surface layer below and the top of the boundary layer above.

14.4 Low-level jets

14.4.1 Formation

The formation of low-level jets requires a temporal or spatial change in the thermal stability of the atmospheric boundary layer which leads to a sudden change between two different equilibria of forces. The flow must transit from an unstable or neutral condition where friction, pressure-gradient and Coriolis forces balance each other to a stable condition where only pressure-gradient and Coriolis force balance each other (see Fig. 14.8). The sudden disappearance of the retarding friction in the equilibrium of forces leads to an inertial oscillation of the horizontal wind vector. Wind speed shoots to much higher values and the increased wind speed leads to a stronger Coriolis force which provokes a turning of the wind vector as well. The relevant equations for the wind components u and v at the moment of the disappearance of the frictional force read:

$$\frac{\partial u}{\partial t} = -f\left(v - v_g\right)$$

(14.17)

$$\frac{\partial v}{\partial t} = f\left(u - u_g\right)$$

(14.18)

where f is the Coriolis parameter und u_g and v_g are the components of the geostrophic wind. The terms on the left-hand side involve a dependence on time. Therefore, the analytical solution of (14.17) and (14.18) describes an oscillation with time, t:

$$u - u_g = D_v \sin ft + D_u \cos ft$$

(14.19)

$$v - v_g = D_v \cos ft - D_u \sin ft$$

(14.20)

where D_u and D_v are the ageostrophic wind components at the beginning of the oscillation in the moment when the retarding frictional force vanishes.

In the temporal domain this corresponds to a sudden change from an unstable daytime convective boundary layer to a nocturnal stable boundary layer. This requires clear skies in order to have rapid changes in thermal stratification but still non-vanishing horizontal synoptic pressure gradients. Therefore, nocturnal low-level jets usually appear at the edges of high-pressure systems (see shaded area in Fig. 14.9).

In the spatial domain this corresponds to a sudden transition of the flow from a surface which is warmer than the air temperature to a smooth surface which is colder than the air temperature. This may happen when the flow crosses the coast line from warm land to a colder ocean surface or from bare land to snow or ice-covered surfaces.

14.4.2 Frequency of low-level jets

It was mentioned in the preceding subchapter that the occurrence of nocturnal low-level jets depends on certain synoptic weather conditions. Therefore, it can be expected that the frequency of occurrence is linked to the appearance of certain weather or circulation types. For Central Europe the "Grosswetterlagen" (large-scale weather types) have proven to give a good classification of the weather situation (Gerstengarbe et al. 1999). Fig. 14.10 shows the frequency of occurrence of low-level jets over Northern Germany as function of these 29 large-scale weather types. The two most relevant types (the two left-most columns in Fig. 14.10) are a high-pressure bridge over Central Europe (type "BM") and a high-pressure area over the British Isles (type "HB"). All in all a low-level jet appeared in 23 % of all nights.

Fig. 14.10 showed the frequency of occurrence of a low-level jet as function of the weather type. The relevance of a certain weather type for the formation of a low-level jet can be assessed when comparing the frequency of low-level jet occurrence with the overall frequency of occurrence of the respective weather type. Fig. 14.11 has been produced by dividing the frequencies shown in Fig. 14.10 by the occurrence frequency of the respective weather types during the same observation period. There are two weather types where the occurrence frequency is identical to the occurrence frequency of the low-level jets during this weather type. This means that in every night when this weather type prevailed a low-level jet was observed. This is indicated by a low-level jet efficiency of 1.0 in Fig. 14.11. Small deviations from unity are due to the limited sample size evaluated for this purpose. These two weather types are "HNFA" and "HFZ" which are both related to high-pressure systems to the North of the investigation site.

Such a high efficiency for forming a low-level jet allows for a quite certain forecast of the occurrence of a low-level jet. Once such weather types are forecasted a low-level jet will form with a very high probability. The values given in Fig. 14.11 can be used to give the low-level jet formation probability for Northern Germany for each of the weather types. For other areas the investigation has to be repeated with local low-level jet data.

14.5 Summary

Wind resources depend on the large-scale weather conditions as well as on the local vertical structure of the atmospheric boundary layer. Ground-based remote sensing is now a viable technique to monitor the vertical structure of the atmospheric boundary layer. Three different techniques are presently available: acoustic sounding (sodars), optical sounding (wind lidars and ceilometers) and the combination of acoustic and electro-magnetic sounding (RASS). Direct detection of MLH from acoustic backscatter intensities is limited to the order of about 1 km due to the rather high attenuation of sound waves in the atmosphere. In contrast, optical remote sensing offers much larger height ranges of at least several kilometres, because the attenuation of light waves in the atmosphere is small unless there is fog, clouds or heavy precipitation. This now offers the possibility to introduce information on boundary layer structure such as mixing-layer height and the frequency of occurrences of low-level jets into the monitoring and description of wind resources.

Notation

a	factor of proportionality
A1	$(B_M + B_U)/2$
A2	$(B_M - B_U)/2$
ABL	atmospheric boundary layer
ARE	acoustic received echo (method)
B_M	mixing-layer mean of $B(z)$
B_U	value of $B(z)$ above the mixing layer
B_{min}	threshold value for $B(z)$
$B(z)$	optical backscatter intensity
$B_i(z)$	idealized optical backscatter intensity
$\partial B / \partial z_{max}$	threshold value for the vertical derivative of $B(z)$
c	speed of light
c_a	RASS speed of sound ($= c_s + w$)
c_s	true speed of sound
CBL	convective boundary layer
D_u	initial ageostrophic wind component
D_v	initial ageostrophic wind component
DR_1	threshold value for the vertical gradient of $R(z)$
DR_2	threshold value for the vertical gradient of $R(z)$
EARE	enhanced acoustic received echo (method)
f	Coriolis parameter
f_a	acoustic frequency
f_e	electro-magnetic frequency
Hn	analysed height (n is a one-digit number)
$H4_{GM}$	height of minimum of vertical gradient of $B(z)$
$H4_{IPM}$	height of minimum of second vertical derivative of $B(z)$
$H4_{LGM}$	height of minimum of logarithmic vertical gradient of $B(z)$
HWS	horizontal wind speed (method)
MLH	mixing-layer height
MLH_{ac}	mixing-layer height from acoustic sounding
MLH_{op}	mixing-layer height from optical sounding
q	specific humidity
R_c	threshold value for $R(z)$
$R(z)$	acoustic backscatter intensity
RASS	radio-acoustic sounding system
t	time
T_a	acoustic temperature
VWV	vertical wind variance (method)
u	horizontal wind component
u_g	horizontal component of geostrophic wind (towards East)
v	horizontal wind component (towards East)
v_g	horizontal component of geostrophic wind (towards North)

w	vertical wind component (towards North)
$W_B(z)$	scale averaged power spectrum profile
z	height above ground
z_i	boundary layer height
Δf_e	Doppler shift of electro-magnetic frequency
Δh	height interval
λ_a	wavelength of sound wave
$\lambda_{a,B}$	wavelength of sound wave fulfilling the Bragg condition
λ_e	wavelength of electro-magnetic wave
σ_w	standard deviation of the vertical wind component
ϑ	potential temperature
ϑ_a	acoustic potential temperature
ϑ_v	virtual potential temperature

References

Angevine W, White AB, Avery SK (1994) Boundary layer depth and entrainment zone characterization with a boundary layer profiler. Bound-Layer Meteorol **68**: 375–385

Asimakopoulos DN, Helmis CG, Michopoulos J (2004) Evaluation of SODAR methods for the determination of the atmospheric boundary layer mixing height. Meteor Atmos Phys **85**: 85–92

Beyrich F (1995) Mixing height estimation in the convective boundary layer using sodar data. Bound-Lay Meteorol **74**: 1-18

Beyrich F (1997) Mixing height estimation from sodar data – a critical discussion. Atmosph Environ **31**: 3941-3954

Beyrich F, Görsdorf U (1995) Composing the diurnal cycle of mixing height from simultaneous SODAR and Wind profiler measurements. - Bound-Layer Meteorol **76**: 387-394

Boers R, Spinhirne JD, Hart WD (1988) Lidar Observations of the Fine-Scale Variability of Marine Stratocumulus Clouds. J Appl Meteorol **27**: 797–810

Bösenberg J, Linné H (2002) Laser remote sensing of the planetary boundary layer. Meteorol Z **11**: 233–240

Brooks IM (2003) Finding boundary layer top: application of a wavelet covariance transform to lidar backscatter profiles. J Atmos Oceanic Technol **20**: 1092-1105

Cohn SA, Angevine WM (2000) Boundary Layer Height and Entrainment Zone Thickness Measured by Lidars and Wind-Profiling Radars. J Appl Meteorol **39**: 1233–1247

Contini, D, Cava, D, Martano, P, Donateo, A, Grasso, FM (2009) Comparison of indirect methods for the estimation of Boundary Layer height over flat-terrain in a coastal site. Meteorol. Z. **18**, 309-320

Davis KJ, Gamage N, Hagelberg CR, Kiemle C, Lenschow DH, Sullivan PP (2000) An objective method for deriving atmospheric structure from airborne lidar observations. J Atmos Oceanic Technol **17**: 1455-1468

de Haij M, Wauben W, Klein Baltink H (2006) Determination of mixing layer height from ceilometer backscatter profiles. In: Slusser JR, Schäfer K, Comerón A (eds) Remote Sensing of Clouds and the Atmosphere XI. Proc. SPIE Vol **6362**: paper 63620R.

Devara PCS, Ernest Ray P, Murthy BS, Pandithurai G, Sharma S, Vernekar KG (1995) Intercomparison of Nocturnal Lower-Atmospheric Structure Observed with LIDAR and SODAR Techniques at Pune, India. J Appl Meteorol **34**: 1375-1383

Emeis, S (2010) Measurement Methods in Atmospheric Sciences. In situ and remote. Series: Quantifying the Environment Vol. 1. Borntraeger Stuttgart. XIV+257 pp., 103 Figs, 28 Tab. ISBN 978-3-443-01066-9

Emeis, S (2011) Surface-Based Remote Sensing of the Atmospheric Boundary Layer. Series: Atmospheric and Oceanographic Sciences Library, Vol. 40. Springer Heidelberg etc., X+174 pp. 114 illus., 57 in color., H/C. ISBN: 978-90-481-9339-4, e-ISBN 978-90-481-9340-0, ISSN 1383-8601, DOI: 10.1007/978-90-481-9340-0

Emeis, S (2012) Wind Energy Meteorology – Atmospheric Physics for Wind Power Generation. Springer Heidelberg etc., in print (to appear in autumn 2012)

Emeis S, Schäfer K (2006) Remote sensing methods to investigate boundary-layer structures relevant to air pollution in cities. Bound-Lay Meteorol **121**: 377-385

Emeis S, Türk M (2004) Frequency distributions of the mixing height over an urban area from SODAR data. Meteorol Z **13**: 361-367

Emeis S, Jahn C, Münkel C, Münsterer C, Schäfer K (2007) Multiple atmospheric layering and mixing-layer height in the Inn valley observed by remote sensing. Meteorol Z **16**: 415-424

Emeis S, Schäfer K, Münkel C (2008) Surface-based remote sensing of the mixing-layer height – a review. Meteorol Z **17**: 621-630

Emeis S, Schäfer K, Münkel C (2009) Observation of the structure of the urban boundary layer with different ceilometers and validation by RASS data. Meteorol Z **18**: 149-154

Engelbart DAM, Bange J (2002) Determination of boundary-layer parameters using wind profiler/RASS and sodar/RASS in the frame of the LITFASS project. Theor Appl Climatol **73**: 53-65

Eresmaa N, Karppinen A, Joffre SM, Räsänen J, Talvitie H(2006) Mixing height determination by ceilometer. Atmos Chem Phys **6**: 1485–1493 available from www.atmos-chem-phys.net/6/1485/2006/

Flamant C, Pelon J, Flamant PH, Durand P (1997) Lidar determination of the entrainement zone thickness at the top of the unstable marin atmospheric boundary-layer. Bound-Layer Meteorol **83**: 247–284

Grimsdell AW, Angevine WM (1998) Convective Boundary Layer Height Measurement with Wind Profilers and Comparison to Cloud Base. J Atmos Oceanic Technol **15**: 1331–1338

Gryning, S.-E., E. Batchvarova, B. Brümmer, H. Jørgensen, S. Larsen (2007) On the extension of the wind profile over homogeneous terrain beyond the surface boundary layer. Bound.-Lay. Meteorol., **124**, 251–268.

Hayden KL, Anlauf KG, Hoff RM, Strapp JW, Bottenheim JW, Wiebe HA, Froude FA, Martin JB, Steyn DG, McKendry IG (1997) The Vertical Chemical and Meteorological Structure of the Boundary Layer in the Lower Fraser Valley during Pacific '93. J Atmos Environ **31**: 2089–2105

Hennemuth B, Kirtzel H-J (2008) Towards operational determination of boundary layer height using sodar/RASS soundings and surface heat flux data. Meteorol Z **17**: 283-296

Hooper WP, Eloranta E (1986) Lidar measurements of wind in the planetary boundary layer: the method, accuracy and results from joint measurements with radiosonde and kytoon. J Clim Appl Meteorol **25**: 990-1001

Lammert A, Bösenberg J (2006) Determination of the Convective Boundary-Layer Height with Laser Remote Sensing. Bound-Lay Meteorol **119**: 159-170

Martucci G, Srivastava MK, Mitev V, Matthey R, Frioud M, Richner H (2004) Comparison of lidar methods to determine the Aerosol Mixed Layer top. In: Schäfer K, Comeron A, Carleer M, Picard RH (eds.): Remote Sensing of Clouds and the Atmosphere VIII. Proc of SPIE **5235**: 447-456

Melfi SH, Spinhirne JD, Chou SH, Palm SP (1985) Lidar Observation of the Vertically Organized Convection in the Planetary Boundary Layer Over the Ocean. J Clim Appl Meteorol **24**: 806–821

Menut L, Flamant C, Pelon J, Flamant PH (1999) Urban Boundary-Layer Height Determination from Lidar Measurements Over the Paris Area. Appl Opt **38**: 945-954

Münkel C, Räsänen J (2004) New optical concept for commercial lidar ceilometers scanning the boundary layer. Proc. SPIE Vol **5571**: 364–374

Neff WD, Coulter RL (1986) Acoustic remote sensing. In: Lenschow DH (ed) Probing the Atmospheric Boundary Layer. Amer Meteor Soc, Boston, MA, 201–239

Peña, A., S.-E. Gryning, C.B. Hasager (2010) Comparing mixing-length models of the diabatic wind profile over homogeneous terrain. Theor. Appl. Climatol., **100**, 325-353.

Piironen AK, Eloranta EW (1995) Convective boundary layer depths and cloud geometrical properties obtained from volume imaging lidar data. J Geophys Res **100**: 25569-25576

Schäfer K, Emeis SM, Rauch A, Münkel C, Vogt S (2004) Determination of mixing-layer heights from ceilometer data. In: Schäfer K, Comeron AT, Carleer MR, Picard RH, Sifakis N (eds.): Remote Sensing of Clouds and the Atmosphere IX. Proc. SPIE Vol **5571**: 248-259

Schäfer K, Emeis S, Junkermann W, Münkel C (2005) Evaluation of mixing layer height monitoring by ceilometer with SODAR and microlight aircraft measurements. In: Schäfer K, Comeron AT, Slusser JR, Picard RH, Carleer MR, Sifakis N (eds) Remote Sensing of Clouds and the Atmosphere X. Proc. SPIE Vol **5979**: 59791I-1 – 59791I-11

Seibert P, Beyrich F, Gryning S-E, Joffre S, Rasmussen A, Tercier P (2000) Review and intercomparison of operational methods for the determination of the mixing height. Atmosph Environ **34**: 1001-1027

Senff C, Bösenberg J, Peters G, Schaberl T (1996) Remote Sesing of Turbulent Ozone Fluxes and the Ozone Budget in the Convective Boundary Layer with DIAL and Radar-RASS: A Case Study. Contrib Atmos Phys **69**: 161–176

Sicard M, Pérez C, Rocadenbosch F, Baldasano JM, García-Vizcaino D (2006) Mixed-Layer Depth Determination in the Barcelona Coastal Area From Regular Lidar Measurements: Methods, Results and Limitations. Bound-Lay Meteorol **119**: 135-157

Steyn DG, Baldi M, Hoff RM (1999) The detection of mixed layer depth and entrainment zone thickness from lidar backscatter profiles. J Atmos Ocean Technol **16**: 953–959

White AB, Senff CJ, Banta RM (1999) A Comparison of Mixing Depths Observed by Ground-Based Wind Profilers and an Airborne Lidar. J Atmos Oceanic Technol **16**: 584–590

Wulfmeyer V (1999) Investigation of turbulent processes in the lower troposphere with water-vapor DIAL and Radar-RASS. J Atmos Sci **56**: 1055-1076

Wulfmeyer, V., and T. Janjić, T., (2005) 24-h observations of the marine boundary layer using ship-borne NOAA High-Resolution Doppler Lidar. J Appl Meteorol **44**: 1723-1744

Figures
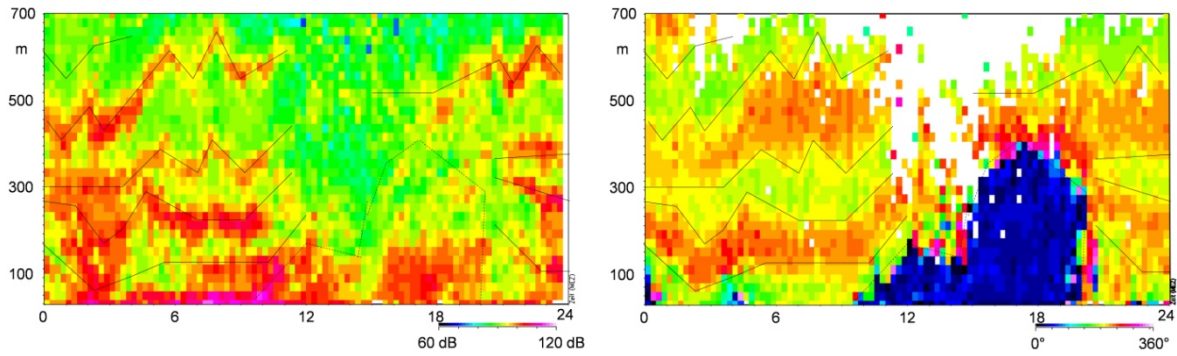
Figure 14.1 Sample time-height cross-section from acoustic sounding with a sodar. Left: acoustic backscatter intensity, right: horizontal wind direction. Thin black lines demark inversions.
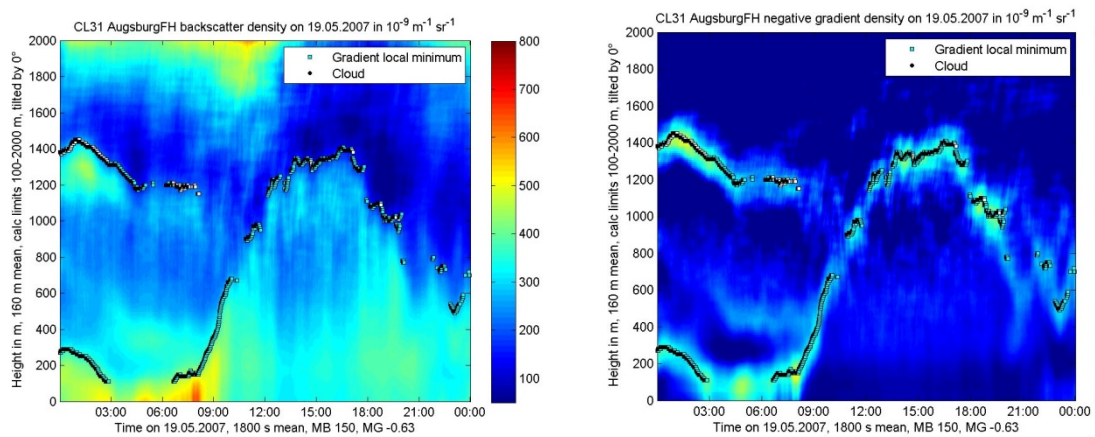
Fugure 14.2 Sample time-height cross-section from optical sounding with a ceilometer. Left: optical backscatter intensity, right: vertical derivative of this backscatter intensity. Dots mark mixing-layer height derived from a gradient algorithm.
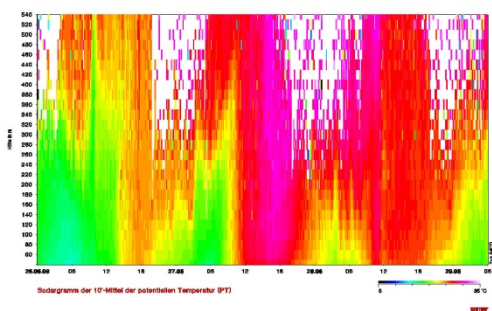

Figure 14.3 Sample time-height cross-section from a potential temperature sounding with RASS
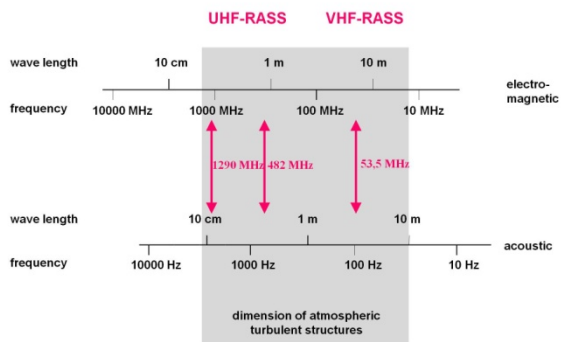
Figure 14.4 Bragg-related acoustic (below) and electro-magnetic (above) frequencies for RASS.
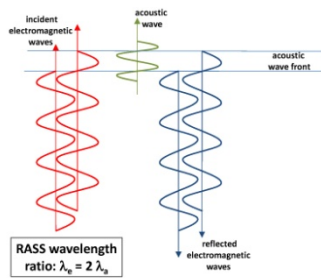
Figure 14.5 Bragg condition for RASS sounding

Figure 14.6 Sodar-RASS. The acoustic antenna is in the middle, the electro-magnetic antennas to the left and right.
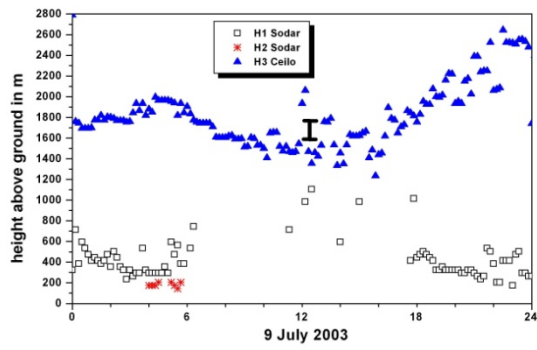
Figure 14.7 Combined sounding with a sodar (black squares and red asterisks) and a ceilometer (blue triangles) giving a complete view of the diurnal variation of the vertical structure of the ABL.
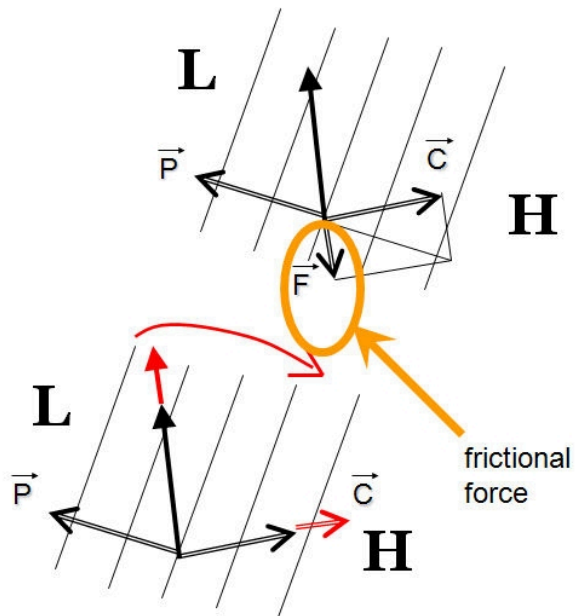

Figure 14.8 Balance of forces before (upper frame) and after (lower frame) the onset of a low-level jet. The red arrows indicate the changes leading to the low-level jet.
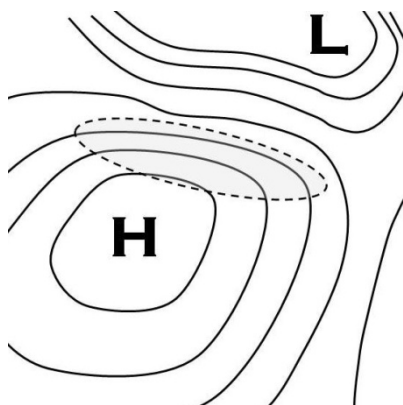

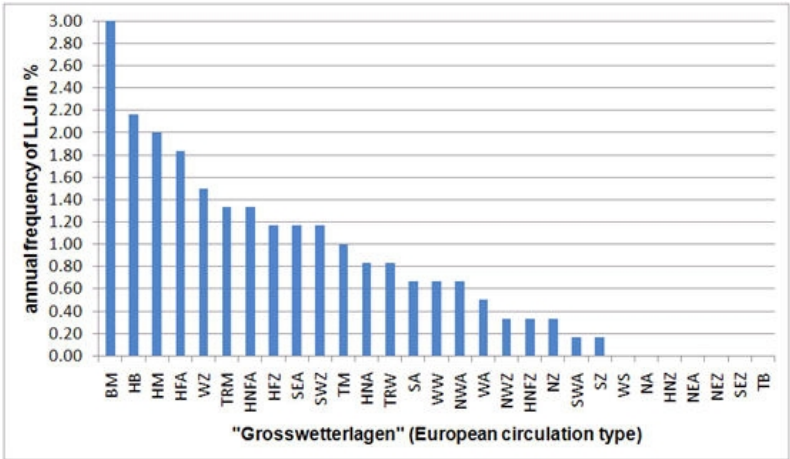Figure 14.9 Favourite regions (shaded area) for the formation of nocturnal low-level jets.

Figure 14.10 Annual frequency of low-level jet events ordered by large-scale synoptic weather patterns (Grosswetterlagen). From two years of SODAR data for Hannover, Germany.
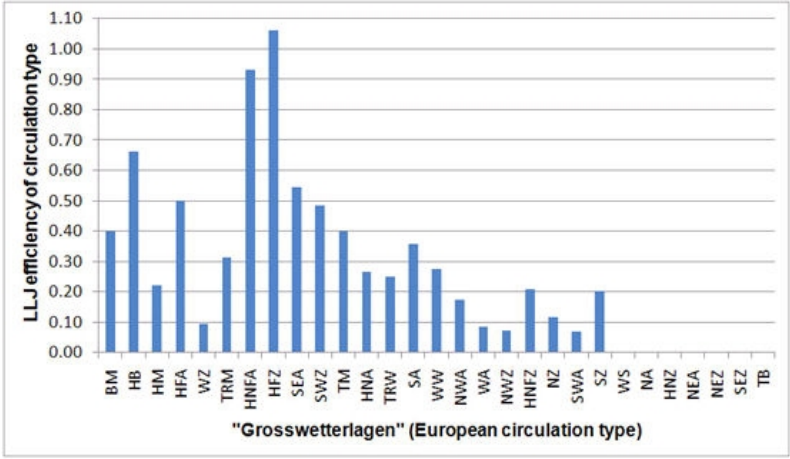

Figure 14.11 Efficiency of a large-scale synoptic weather pattern (Grosswetterlage) to form a low-level jet. From two years of SODAR data for Hannover, Germany.